Experimental and theoretical L-subshell ionization cross sections for $_{83}$Bi by electron impact from the L_3 threshold to 100 keV

Suelen F. Barros [1,2,*] Vito R. Vanin [2] Nora L. Maidana [2] Alexandre A. Malafronte,[2]
José M. Fernández-Varea [3,2] and Michael S. Pindzola[4]

[1]*Instituto Federal de São Paulo, Rua Primeiro de Maio 500, Bairro Estação, CEP:08571-050 Itaquaquecetuba, SP, Brazil*
[2]*Universidade de São Paulo, Instituto de Física, Rua do Matão 1371, Cidade Universitária, CEP:05508-090 São Paulo, SP, Brazil*
[3]*Universitat de Barcelona, Facultat de Física (FQA and ICC), Diagonal 645, ES-08028 Barcelona, Catalonia, Spain*
[4]*Auburn University, Department of Physics, Auburn, Alabama 36849, USA*

We report experimental and theoretical Bi L_1, L_2, and L_3 subshell ionization cross sections by the impact of electrons with energies from the Bi L_3 ionization threshold to 100 keV. The x-ray spectra have been acquired with two Si drift detectors placed in vacuum, which allowed us to better evaluate the peak fit procedure in the L multiplet. The $L\alpha$, $L\beta$, $L\gamma$, $L\ell$, and $L\eta$ x-ray production cross sections, measured with relative uncertainties ranging from 5% to 9%, and two sets of atomic relaxation parameters have been used to derive the Bi L_1, L_2, and L_3 ionization cross sections. Although the experimental uncertainties of the subshell ionization cross sections are smaller than those of the few previous measurements, they remain large due to the uncertainties associated with the relaxation parameters. Furthermore, ionization cross sections have been calculated for the three L subshells with the subconfiguration average distorted-wave (SCADW) formalism, which includes the full two-body retarded electromagnetic interaction between the projectile and target electrons. These theoretical cross sections are 15% to 30% lower than the measured values, but the agreement is reasonable given the aforementioned high uncertainties. We have also found that the simpler distorted-wave Born approximation yields subshell ionization cross sections that match those computed with the SCADW method.

I. INTRODUCTION

The determination of accurate cross sections for atomic inner-shell ionization by electron impact is of great relevance in several applied fields such as electron-probe microanalysis, electron energy-loss spectroscopy, Auger electron spectroscopy, plasma physics, medical physics, and in general for the simulation of radiation transport in matter [1–3]. Accurate ionization cross-section data are also required in the study of laser-driven inertial confinement fusion [4,5]. Moreover, they are of fundamental interest in basic physics research to help unravel the dynamics of electron-atom ionizing collisions [6].

The measurement of ionization cross sections has been the subject of research for at least 80 years, and the interest extends into the present day [7–15]. In spite of this continued effort, the review by Llovet *et al.* [6] makes it evident that the experimental and theoretical knowledge about the dependence of the ionization cross sections on the atomic number and on the electron energy is still incomplete. The existing data are affected by large uncertainties, and notable discrepancies are found between the published values which are, in most cases, larger than the quoted uncertainties. Significant disagreement is sometimes observed between measurement and theory. Besides, most of the available experimental information is for the K shell. The number of papers dealing with the L shell is increasing, but many of them only provide x-ray production

cross sections and not L subshell ionization cross sections. The situation for the M subshells is also far from being satisfactory [6].

In addition to the difficulties inherent to the absolute measurement of inner-shell ionization cross sections [16], a vacancy in some L or M subshell can be created not only by direct ionization, but also by nonradiative Coster-Kronig transitions between the subshells. Hence, to determine subshell ionization cross sections it is necessary to measure the intensities of a number of characteristic x-ray lines, some of which cannot be clearly resolved in the energy spectra or may have very low intensities. Furthermore, the L and M fluorescence yields and Coster-Kronig coefficients are generally affected by large uncertainties, which propagate to the derived subshell ionization cross sections. Thus, the comparison of experimental results with theory is always mediated by the values and uncertainties of these atomic relaxation parameters.

From the theoretical point or view, ionization cross sections can be calculated by means of semiempirical formulas or *ab initio* approaches [2,6]. Among the latter, the subconfiguration average distorted-wave (SCADW) method developed by Pindzola *et al.* [17,18] includes the full two-body retarded electromagnetic interaction between the projectile and target electrons and uses relativistic distorted plane waves for all free-electron states. In turn, the distorted-wave Born approximation (DWBA) of Bote and Salvat [19], formulated in the Coulomb gauge, employs distorted plane waves for the longitudinal term of the electron-electron interaction and plane waves to simplify the transverse term.

*suelen.barros@ifsp.edu.br; suelenb@if.usp.br

Pindzola [20] has shown recently that the SCADW formalism is in accord with the experimental Au K ionization cross sections. Santos *et al.* [13] measured the K-shell ionization cross section of $_{52}$Te, $_{73}$Ta, and $_{83}$Bi up to 100 keV and compared these data to SCADW calculations, finding again excellent agreement. The DWBA had difficulties for heavy atoms, and this was attributed to the simplified transverse term close to the threshold. On the other hand, for L-subshell ionization the situation remains inconclusive and deserves more experimental and theoretical investigation. In particular, the DWBA and SCADW approaches yield almost identical cross sections for the elements for which both have been calculated, but the comparison with the experimental data is restricted to just two elements [20,21]. The theoretical $_{79}$Au L_1, L_2, and L_3 ionization cross sections were compared with the measurements of Rahangdale *et al.* [10], and exhibit a surprising discrepancy for the L_1 subshell, which was not reproduced in a more recent experiment [12].

Motivated by this challenging context, the purpose of this paper is to furnish new experimental and theoretical Bi L subshell ionization cross sections. This element has been picked for three reasons. First, owing to the high atomic number of $_{83}$Bi it is expected that the transverse term in the DWBA will have a larger influence on the calculated ionization cross section than in the case of $_{79}$Au, and then the difference between the predictions of the DWBA and SCADW formalisms might be slightly larger than that observed for the Au L subshells. Another consequence of the higher atomic number of $_{83}$Bi is that the L x-ray peaks in the spectra can be better resolved by the employed spectrometer, thereby the uncertainties associated with the peak area estimates should be smaller. Finally, the existing data for Bi L are limited to either 17–40 keV [22–24] or 60 keV, 100 keV, and above 200 keV [25–28], and only one of these publications [28] presents absolute Bi L_1, L_2, and L_3 subshell ionization cross sections.

Aside from the improvements already implemented in the experimental arrangement of the previous papers by our research group [12,13,29], the measurements reported here have been done using two detectors simultaneously to better evaluate the fit procedure at two intensities of the continuous component in the spectra, and with both detectors placed in vacuum. Our measurements range from the Bi L_3 ionization threshold up to 100 keV and, therefore, cover the energy interval where the L-subshell ionization cross sections increase, reach a maximum, and start to decrease slowly. Theoretical Bi L_1, L_2, and L_3 ionization cross sections have also been computed within the SCADW formalism.

II. EXPERIMENT

The Bi L_1, L_2, and L_3 subshell ionization cross sections have been measured from the respective ionization thresholds to 100 keV in the (10–100) keV beam line of the São Paulo Microtron [16], using a thin Bi_2O_3/C target. The cross sections have been determined from the characteristic L x-ray yields measured with two Si drift detectors (SDDs), one located at a front angle and another at a back angle relative to the incident electron beam direction. The experimental set-up is similar to those of our former measurements of K and L (sub)shell ionization cross sections and alignment parameter
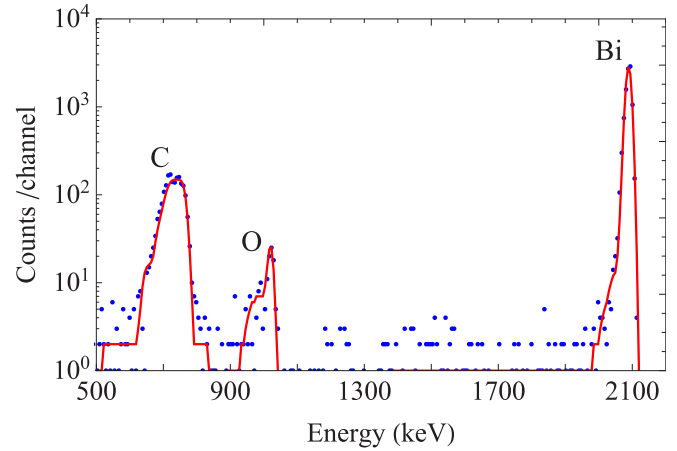

FIG. 1. Experimental (blue dots) and simulated (red curve) energy spectra of ions backscattered elastically from the Bi_2O_3/C target, irradiated with the 2200(11) keV $^4He^+$ beam. The energy dispersion is 6.23 keV/channel.

A_{20} by electron impact [12,13,30], and it is described in detail elsewhere [16].

A. Sample preparation and characterization

The Bi_2O_3/C target has been manufactured by the vapor deposition technique. The target material, Bi_2O_3, is deposited on a thin C substrate, which is attached to a rectangular frame with dimensions of $30 \times 15 \times 0.5$ mm^3 and a circular central opening 10 mm in diameter. First, the hollow frame is covered with a thin C film, and then Bi_2O_3 is deposited in the central area of the frame, on the thin C backing, using a circular mask, 8 mm in diameter, centered in the frame. The frame is made of C fiber to reduce bremsstrahlung by the electron beam halo, and the Bi_2O_3 film occupies an area smaller than the central opening of the frame so as to minimize ionization by stray photons and electrons.

The areal densities (number of atoms per unit surface) of Bi and O atoms in the Bi_2O_3 film, $\mathcal{N}_{Bi} d$ and $\mathcal{N}_O d$, respectively, have been estimated by Rutherford backscattering spectrometry; $\mathcal{N}_{Bi}$ and $\mathcal{N}_O$ are the corresponding numbers of atoms per unit volume and d is the film thickness. The measurements have been carried out at the LAMFI/IFUSP Pelletron tandem accelerator [31]. The target, placed at the center of the irradiation chamber and tilted $7°$ relative to the direction of the incident beam, has been irradiated with a 2200(11) keV $^4He^+$ beam, around 1.8 mm in diameter, hitting its center. The energy spectra of the elastically backscattered ions were recorded by a surface barrier Si detector positioned at $120°$ relative to the ion beam direction. The areal densities have been deduced from the acquired spectra having recourse to the MULTISIMNRA program [31], which is based on SIMNRA calculations [32]. Figure 1 shows one of the energy spectra of backscattered $^4He^+$ particles and the corresponding MULTISIMNRA spectrum.

The uncertainties of the areal densities estimated with the procedure described above have various sources; some of them have been addressed in Ref. [13]. A first group encompasses the beam energy value, electronics gain and

offset, charge integration, scattering angle, and stopping power values; for this target the combined uncertainties amount to 3.5%. In a second group we have the uncertainty associated with the procedure used to estimate the areal density from the spectrum measured with a given counting statistics, which is provided by MULTISIMNRA [31], and for the target of this work it was approximately 0.6%. Besides, there is a third group associated with the inhomogeneities in the thickness of the Bi_2O_3 film. To estimate this value, measurements with the 2200(11) keV $^4He^+$ beam have been made in five different positions of the target: above, below, to the right, and to the left of the target center, in addition to the measurement performed in the center of the target. The standard deviation of these values, 0.40×10^{15} Bi atoms/cm^2, provided an estimate of the uniformity of the film. Since during the irradiation the electron beam also impinges on the center of the target, and both the electron and the $^4He^+$ beam spots have almost the same diameter, the areal density of Bi atoms has been estimated with the measurement done in the central position of the beam, and its uncertainty has been calculated as the square root of the sum of the variances pertaining to the aforementioned contributions. The outcome is $\mathcal{N}_{Bi} d = 15.9(7) \times 10^{15}$ Bi atoms/cm^2, which would correspond to a mass thickness of pure Bi equal to 5.51(24) μg/cm^2. The mass thickness of the C backing is 12.94(11) μg/cm^2; however, this value is not needed for the data analysis below.

As a cross-check, we have calculated $\mathcal{N}_{Bi}/\mathcal{N}_O$ from the estimates of $\mathcal{N}_{Bi}$ and $\mathcal{N}_O$ obtained by analyzing the backscattered ion spectra. The value found was 0.69(7), compatible with the ratio $\frac{2}{3}$ expected for Bi_2O_3. Although the manufactured target is not of pure Bi, the atomic number of $_8O$ is an order of magnitude lower than that of $_{83}Bi$. Therefore, the increase in the production of bremsstrahlung in the Bi_2O_3/C target caused by the presence of O is negligible within the uncertainty bars of this paper so that it has been disregarded.

B. Irradiation chamber and detection system

In the São Paulo Microtron accelerator the electrons emitted by the accelerator gun, with kinetic energy between 10 and 100 keV, are deflected by a dipole magnet towards the irradiation chamber.

The irradiation chamber is cylindrical, it has an internal diameter of 490 mm, 220 mm in height, side walls made of stainless steel, and upper and lower covers of Al. At 0° relative to the incident beam direction there is a conical Faraday cup made of graphite, shaped as a truncated cone with a half-aperture angle of 12°, and 200 mm deep. The Faraday cup and the irradiation chamber are electrically insulated, and two current integrators connected to them collect the incident electrons.

The x-ray spectrometers can be fixed to any of the 13 mounting flanges available, either outside or inside the irradiation chamber. The x rays emitted from the target have been detected *simultaneously* by two SDDs (Amptek, Bedford, USA), placed at 48.9(5)° and 149.1(5)° relative to the beam direction. The SDDs were inside the vacuum chamber,

293(2) mm away from the target, to reduce the attenuation of the x rays by the spectroscopy windows. According to the manufacturer's specifications, the SDD consists of a 0.5-mm-thick Si crystal with a frontal area equal to 25 mm^2. The area of the internal collimator is 17 mm^2, the detector is covered by a 12.7-μm-thick Be window, separated by 1.4 mm from the front surface of the active volume, and it has a dead layer whose thickness is around 0.15 μm. The energy resolution, full width at half-maximum (FWHM), of the two SDDs for the Fe $K\alpha$ x rays (6.4 keV) are 133 and 136 eV for the SDDs placed at the front and back angle, respectively. The charge pulses from the current integrators have been counted by SDD internal scalers gated by their respective multichannel analysis (MCA) logical signals.

The internal parts of the flanges where the detectors were placed have been equipped with Al cylindrical collimators, 9 mm in diameter and 70 mm in length, coupled to the camera. The SDDs have been embedded in these internal collimators to limit the area of the chamber internal wall that is visible to the detectors, without reducing their active area. Moreover, the area of chamber diametrically opposite the detectors, which is visible through them, has been covered with 100-μm-thick aluminized Kapton, reducing in this way the bremsstrahlung radiation generated when scattered electrons reach the inner wall of the chamber.

The γ rays and x rays emitted by certified ^{57}Co, ^{133}Ba, and ^{241}Am radioactive sources that were prepared and had their activities calibrated at the Nuclear Metrology Laboratory, Research Institute and National Commission for Nuclear Energy, São Paulo, have been utilized to calibrate the detectors in energy, with standard energies taken from Ref. [33], and also to determine the full-energy (FE) peak efficiency. Details on how these sources have been manufactured can be found in Ref. [16]. Briefly, a C fiber frame that is identical to those on which the targets are mounted is covered with a 7.5-μm-thick Kapton foil. The carrier-free radioactive material is then deposited in the center of the frame, between two thin films of collodion, on the Kapton foil, forming a spot around 4 mm in diameter. Finally, a second Kapton foil is used to seal the collodion with the radioactive material.

The FE peak efficiency ε_{FE} of the two spectrometers has been established from the net areas of several γ-ray and x-ray peaks in the acquired spectra when the radioactive sources are placed in the center of the irradiation chamber at the same position occupied by the target during the irradiations [34]. Notice that during the calibration measurements with the radioactive sources the chamber is filled with air, unlike the target irradiation conditions, when the chamber is evacuated. An analytical model for the FE peak efficiency [35] had been carefully assessed for SDDs in Ref. [34], and it was adopted to compute ε_{FE} in previous experiments with these spectrometers [12]. In this model, the fitted parameters are the fraction of solid angle subtended by the detector $\Omega/(4\pi$ sr) and the thickness $\mathcal{L}$ of the Si crystal. The values estimated by the fit in this experiment are $\Omega/(4\pi$ sr$) = 1.642(18) \times 10^{-5}$ and $\mathcal{L} = 0.495(16)$ mm for the detector at 48.9(5)°, and $\Omega/(4\pi$ sr$) = 1.564(14) \times 10^{-5}$ and $\mathcal{L} = 0.498(15)$ mm for the detector at 149.1(5)°. Figure 2 depicts the experimental
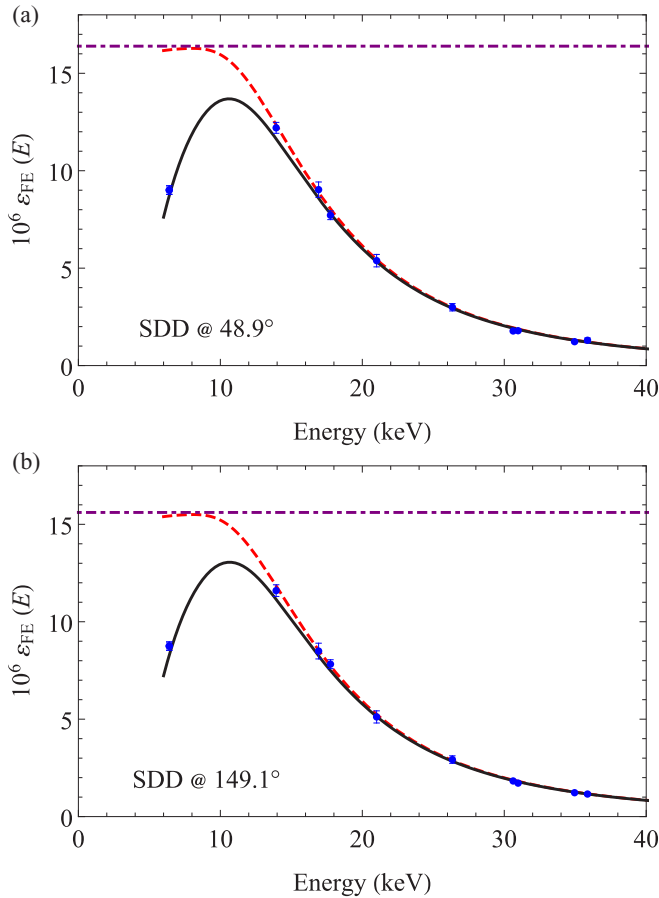
FIG. 2. FE peak efficiency ε_{FE}, multiplied by 10^6, of the SDDs placed at (a) $\theta_1 = 48.9(5)°$ and (b) $\theta_2 = 149.1(5)°$, relative to the beam direction, as a function of photon energy. The symbols with uncertainty bars (1 standard deviation) are the experimental values. The curves are the FE peak efficiencies calculated with the fitted parameters $\Omega/(4\pi\ \mathrm{sr})$ and $\mathcal{L}$. The solid curves account for attenuator thicknesses (air, Kapton) appropriate to the calibration with certified radioactive sources (chamber filled with air), whereas the dashed ones pertain to the electron-beam irradiation conditions (vacuum in chamber). The dotted-dashed horizontal lines indicate the geometrical efficiencies $\Omega/(4\pi\ \mathrm{sr})$.

FE peak efficiency values together with the $\varepsilon_{FE}(E)$ curves calculated with the fitted parameters in the analytical model and the attenuating layers appropriate to the two experimental configurations, i.e., during the measurements with radioactive sources (the chamber is filled with air at atmospheric pressure) and during the irradiations (the chamber is evacuated to a pressure of 7×10^{-5} Pa).

The analytical model calculated with the fitted parameters, and including the appropriate attenuators, namely, the thickness of the Be window and the thickness of the Si dead layer, is used to evaluate the FE peak efficiency in the irradiation condition.

During the irradiations the target has been positioned in the center of the irradiation chamber, perpendicular to the direction of the incident beam. The spot of the electron beam remained around 2 mm in diameter. The irradiations have been carried out at 18 electron energies ranging from the Bi L_3
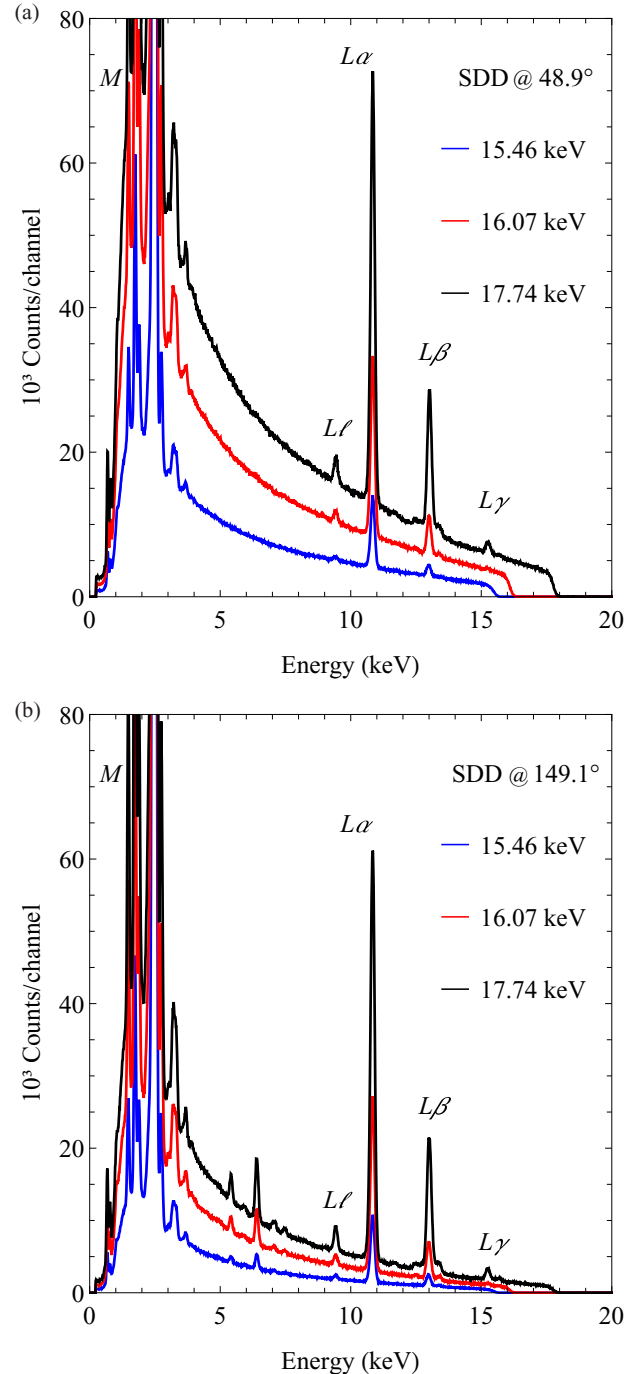

FIG. 3. X-ray spectra measured with the SDDs placed at (a) 48.9(5)° and (b) 149.1(5)° relative to the incident beam direction. The spectra from bottom to top correspond to electron energies of 15.46(6) keV (blue curves), 16.07(7) keV (red curves), and 17.74(5) keV (black curves), respectively, in accordance with the Duane-Hunt law. The energy dispersion is 12.77 eV/channel for the detector at 48.9(5)° and 12.69 eV/channel for the detector at 149.1(5)°.

ionization threshold to 100 keV, with some values strategically chosen between the ionization thresholds of the three L subshells. Figure 3 displays spectra that have been recorded at 15.46(6) keV (only the L_3 subshell can be ionized), 16.07(7) keV (now the L_2 subshell can also be ionized), and 17.74(5)

keV (the three subshell ionization channels are open), for both detectors.

The incident current has been selected between 900 nA and 6 μA to keep the dead time below 10%. Then, the acquisition rates have varied between 2 and 13 kHz, and the irradiations have lasted from 600 to 1200 s. The total charge impinging on the target has been measured directly with an accuracy better than 0.5%, evaluating the sum of the charges collected in the Faraday cup and in the irradiation chamber during the measurement time of each spectrum. The dead times have been estimated following Ref. [36], and their relative uncertainties are around 2% for the quoted acquisition rates.

III. DATA ANALYSIS

A. Estimate of the electron-beam energy

For the energies from the Bi L_3 ionization threshold to 50 keV, the electron-beam energies and their uncertainties have been estimated from the fit of the parameters of an analytical model to the bremsstrahlung spectrum tip [37]. This model is built from the convolution of the detector's response function, taking into account its FE peak efficiency, with the theoretical bremsstrahlung spectrum emitted by the target [38,39]. The model parameters are the average and the width of the electron-beam energy distribution and the bremsstrahlung yield, and they have been fitted to the experimental bremsstrahlung spectrum in the tip region. For energies above 50 keV, the value provided by the voltmeter connected to the electron gun has been employed because the FE peak efficiency of the SDDs decreases rapidly (Fig. 2).

B. Fitting procedure to estimate the x-ray peak areas

The *L* x-ray spectra have been fitted with the procedure described in Ref. [30]. The parameters of the entire *L* multiplet, which extends from the $L\ell$ line to the $L\gamma$ group, have been fitted simultaneously to the net spectrum obtained after subtracting from the measured spectrum the contributions of pileup [36], Si K x-ray escape [35], and an approximate bremsstrahlung component underneath the *L* multiplet [37]. The latter has been calculated with the parameters fitted in the procedure used to estimate the electron-beam energy (below 50 keV) or with the experimental mass thickness of the Bi_2O_3 film and the energy measured with the voltmeter (above 50 keV). Figure 4 shows the experimental spectra for the irradiation with 27.92(5) keV electrons and the extrapolation of the curves calculated with the parameters fitted to the tip of the bremsstrahlung spectra.

The model function adopted to estimate the peak areas is the sum of a Voigt function with a smoothed step for each characteristic x-ray line, and a second-degree polynomial to account for the remaining part of the continuous component. The Voigt function results from the convolution of the response function of the spectrometer (a Gaussian) with the natural shape of an x-ray line (a Lorentzian) (see Ref. [34] and references cited therein). The Gaussian dispersion, associated with the detector FWHM, is a function of photon energy E given by $\sqrt{s_{el}^2 + W_{Si} F_{Si} E}$ [35], where the parameter s_{el} is the standard deviation of the electronic noise introduced by
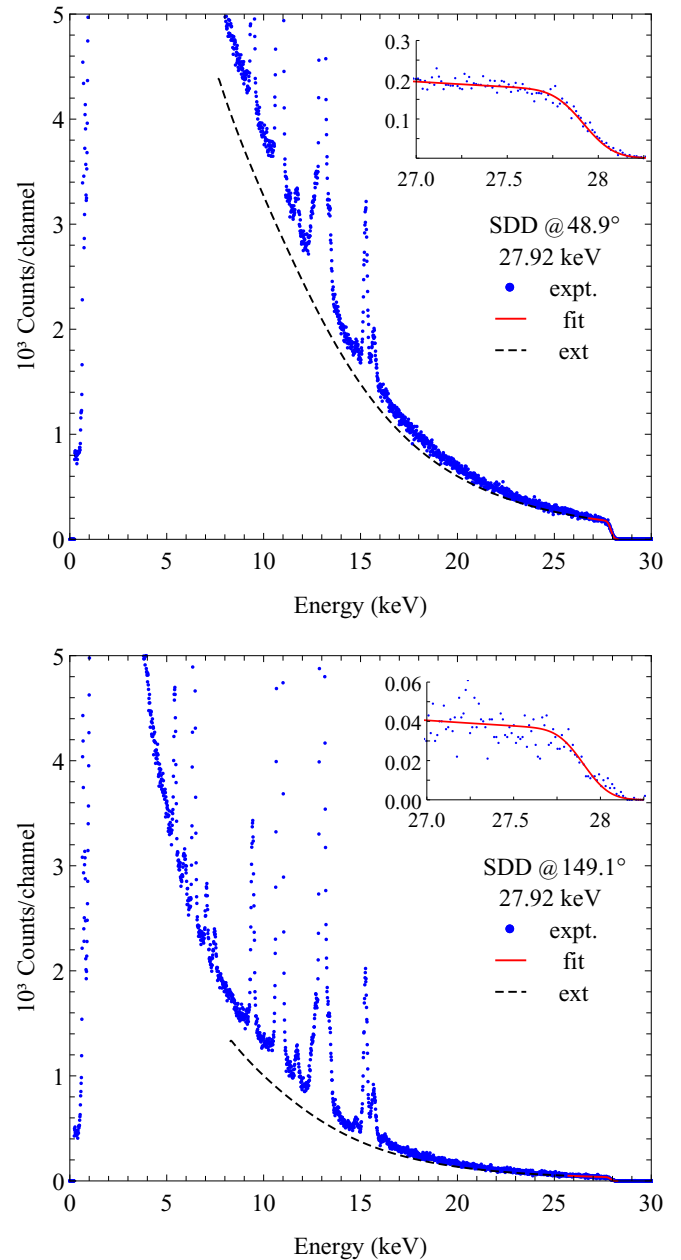

FIG. 4. Bremsstrahlung component under the *L* multiplet, emitted by the Bi_2O_3/C target bombarded with 27.92(5) keV electrons, calculated with the parameters fitted to the tip of the spectrum. The (blue) dots denote the experimental spectra, the (red) continuous curves are the values calculated with the theoretical model and the fitted parameters, and the (black) dashed curves correspond to the theoretical curve extrapolated outside the fit region.

the pulse amplification process, whereas W_{Si} and F_{Si} are the average energy expended in the formation of an electron-hole pair in Si and the Fano factor [40], respectively. The product $W_{Si} F_{Si}$ has been set equal to the value fitted to the peaks in the calibration process with the radioactive sources and s_{el} has been treated as an adjustable parameter for each run. In turn, for the natural width of the Lorentzian profile we resorted to the values extracted from Ref. [41] and the spectrometer's energy dispersion.

The parameters of the peaks in the $L\alpha$, $L\beta$, and $L\gamma$ multiplets, along with those of the Lt, Ls, $L\ell$, and $L\eta$ lines, have been fitted simultaneously in one step (the nomenclature of the L characteristic x rays is given in Table II below). To this end, the L multiplet has been split into three blocks, and in each of them the positions of one or more peaks have been regarded as free parameters whereas those of the other peaks have been fixed relative to the former. The Lt and Ls lines, which correspond to L_3M_2 and L_3M_3 transitions, respectively, are forbidden in the dipole approximation but appear discreetly in the spectra. These lines have been included in the fit procedure because they influence the parameters of the continuous component.

In the first block, the positions of the $L\ell$, $L\alpha_1$, and $L\eta$ peaks have been treated as free parameters, whereas the positions of the Lt, Ls, and $L\alpha_2$ lines have been fixed relative to the $L\alpha_1$ peak. In the second one, the $L\beta_6$, $L\beta_4$, $L\beta_1$, and $L\beta_5$ peak positions have been considered as adjustable parameters, while the positions of the $L\beta_2$, $L\beta_3$, $L\beta_9$, $L\beta_{10}$, and $L\beta_{15}$ lines have been kept fixed relative to the $L\beta_1$ position. Finally, in the third block, the $L\gamma_5$, $L\gamma_1$, and $L\gamma_4$ peak positions have been left as free parameters, and the $L\gamma_2$, $L\gamma_6$, and $L\gamma_3$ peaks had their positions fixed relative to the $L\gamma_1$ peak position. The relative positions chosen for these parameters have been determined from the experimental radiative transition energies compiled by Deslattes and coworkers [33], and the spectrometer's energy dispersion.

The Lt, Ls, $L\beta_{15}$, and $L\gamma_6$ peak areas have been fixed with respect to the $Lt/L\alpha_1$, $Ls/L\alpha_1$, $L\beta_{15}/L\alpha_1$, and $L\gamma_6/L\gamma_1$ relative intensity ratios, respectively, using the values tabulated in Ref. [42] for the first two peaks and in Ref. [43] for the others, after correcting for the spectrometer FE peak efficiency. The areas of the remaining peaks have been regarded as free parameters in all fits. The net experimental energy spectra corresponding to the irradiation with a 27.92(5) keV electron beam, Fig. 4, are plotted in Fig. 5 together with the curves calculated with the fitted parameters.

A few ratios of peak areas, corrected for the FE peak efficiency, have been calculated to assess whether the continuous component of the spectrum has been properly fitted, as well as to verify whether some peaks have been correctly resolved in the fit. Since the largest uncertainties in the x-ray production cross sections come from the areal density of Bi atoms and from the FE peak efficiency, the relative peak areas can be determined with higher precision. Specifically, we have evaluated $A_{L\alpha_2}/A_{L\alpha_1}$, whose peaks result from transitions to the L_3 subshell, $A_{L\eta}/A_{L\beta_1}$ and $A_{L\gamma_5}/A_{L\gamma_1}$, which come from transitions to the L_2 subshell, and $A_{L\gamma_{4,4'}}/A_{L\beta_4}$ and $A_{L\gamma_2}/A_{L\beta_3}$, which involve transitions to the L_1 subshell. Figure 6 displays these experimental ratios and the ratios of emission rates tabulated in Refs. [42,43]. There is good agreement between the ratios of peak areas measured with the two spectrometers, and also between the experimental ratios and the theoretical values from Refs. [42,43]. This confirms that the procedure implemented to fit the L multiplet has allowed us to correctly separate some lines from the $L\beta$ and $L\gamma$ multiplets that are not completely resolved by the SDDs, and that we have properly dealt with the continuous component of the spectra at both detection angles.
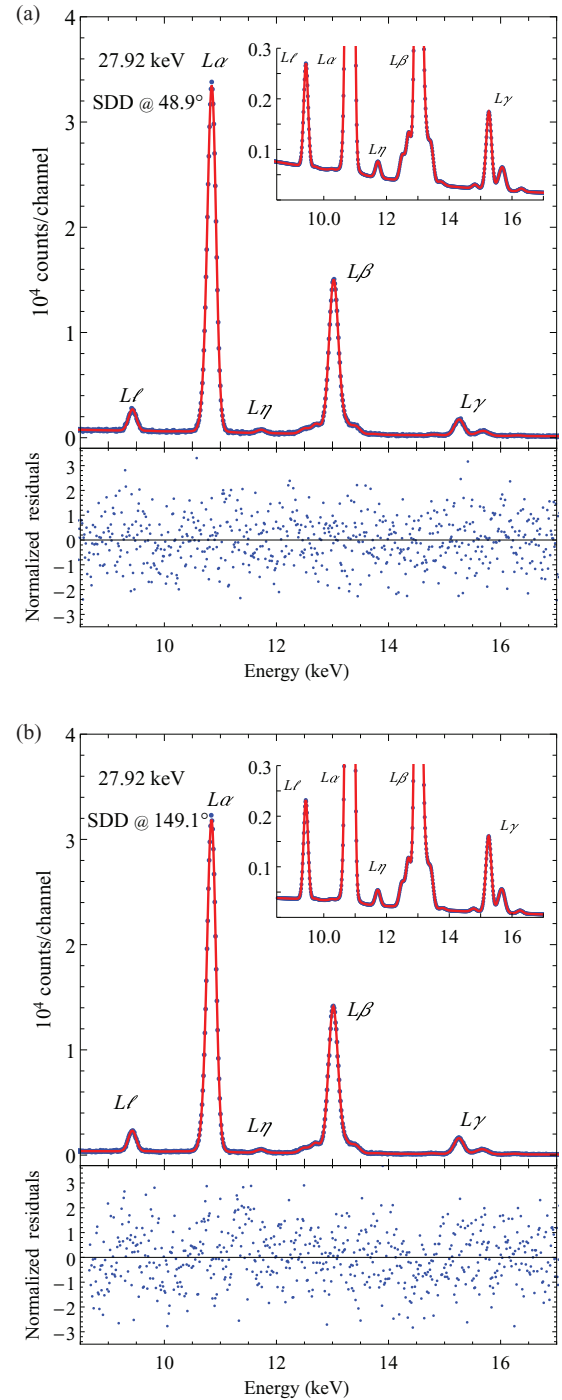

FIG. 5. Experimental spectra (blue dots) after removal of pileup, Si K escape, and the evaluated bremsstrahlung distributions, and model function (red continuous curves) calculated with the fitted parameters for the Bi L multiplet, in the run with 27.92(5) keV electrons, at detection angles of (a) 48.9(5)° and (b) 149.1(5)°.

C. *L* x-ray production cross sections

The x-ray production cross sections have been determined from the expression

$$\sigma_{Lj}^{\mathrm{x}}(E) = \frac{N_{Lj}}{N_\mathrm{e}\,\mathcal{N}_\mathrm{Bi}d_\mathrm{eff}\,\varepsilon_\mathrm{FE}(E_{Lj})\,(1-\phi)}, \quad (1)$$

FIG. 7. Multiplicative correction factor to determine the effective path length of electrons that impinge perpendicularly on the 5.51(24)-μg/cm^2-thick Bi$_2$O$_3$ film as a function of their kinetic energy.

with N_{Lj} the net area of the Lj peak at energy E_{Lj}, N_e the number of incident electrons, $\mathcal{N}_{Bi}$ the number of Bi atoms per unit volume, d_{eff} the effective thickness of the Bi$_2$O$_3$ film (see below), and ϕ the dead time fraction during the acquisition.

Despite the fact that the Bi$_2$O$_3$ film is very thin, the effective path length d_{eff} of the electrons within the film is slightly longer than its thickness d. This is because when the electrons move through the target they experience elastic (and inelastic) collisions that change their direction of flight. To correct for this energy-dependent path length increase, Monte Carlo simulations have been done utilizing the program that was developed in Ref. [30] to estimate the attenuation of the anisotropy parameter caused by the opening of the electron beam inside the target. The program is written in *Mathematica* and implements elastic differential and integrated cross sections from Ref. [44]. Figure 7 presents the simulated correction factor $d_{eff}(E)/d$ for the Bi$_2$O$_3$ film. Supplementary Monte Carlo simulations were carried out with the general-purpose code PENELOPE [3], and the differences between the two sets of simulations enabled an estimation of the $d_{eff}(E)/d$ uncertainties.

The emission of the characteristic L x rays has been assumed to be isotropic even when these originate from vacancies in the L_3 subshell [30,45]. This is because although the characteristic x rays that originate from vacancies in the L_3 subshell are emitted anisotropically, the anisotropy is small (around 6% in the case of the $L\ell$ line, which has the largest anisotropy), and it decreases with the electron energy [30,45]. Since the intensity of the $L\ell$ peak is very weak in comparison with the intensities of the $L\alpha$, $L\beta$, and $L\gamma$ multiplets, and our x-ray production cross sections have uncertainties also around 6%, the effects of anisotropic x-ray emission are within 1 standard deviation so that they have been neglected here.

D. L-subshell ionization cross sections

The experimental Bi L_1, L_2, and L_3 subshell ionization cross sections have been determined from the x-ray production cross sections of the following lines and multiplets (in order of increasing energy): $L\ell$, $L\alpha$, $L\eta$, $L\beta_6$, $L\beta_4$,
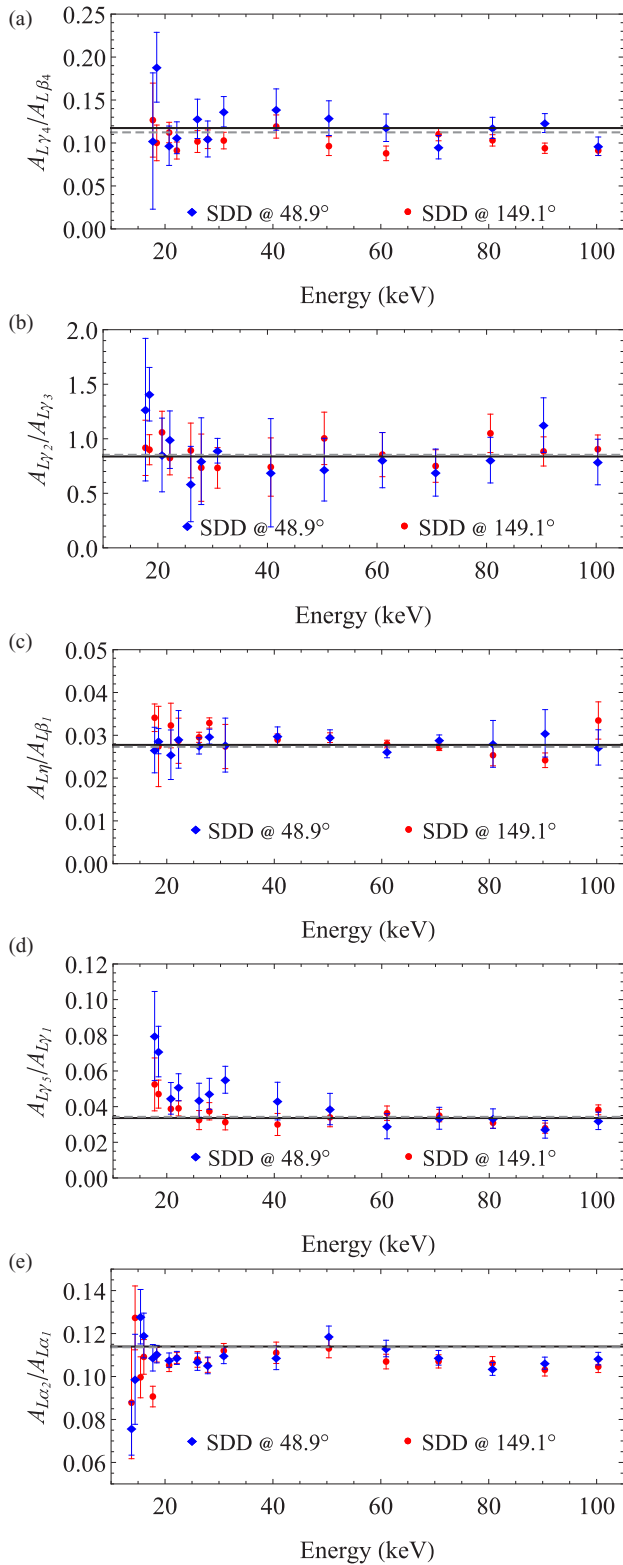
FIG. 6. Experimental ratios (a) $A_{L\gamma_{4,4'}}/A_{L\beta_4}$, (b) $A_{L\gamma_2}/A_{L\gamma_3}$, (c) $A_{L\eta}/A_{L\beta_1}$, (d) $A_{L\gamma_5}/A_{L\gamma_1}$, and (e) $A_{L\alpha_2}/A_{L\alpha_1}$, where A is the experimental peak area corrected for the FE peak efficiency. The symbols represent the data obtained with the SDDs placed at 48.9(5)° (blue diamonds) and 149.1(5)° (red circles) relative to the electron beam direction. The horizontal lines indicate the ratios tabulated by Scofield [42] (black dashed line) and by Campbell and Wang [43] (black continuous line).
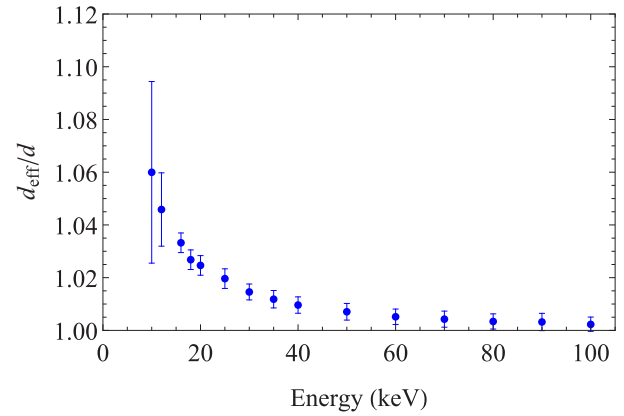
$L\beta_5$, $L\beta_{15,2,1,3,10,9}$, $L\gamma_5$, $L\gamma_1$, $L\gamma_{2,3,6}$, and $L\gamma_{4,4'}$. These x-ray production cross sections can be written in terms of the vacancy-production cross sections $\sigma_{L_i}^{\mathrm{h}}$ as

$$\sigma_{L\ell}^{\mathrm{x}} = \frac{\Gamma_{L_3 M_1}}{\Gamma_{3,\mathrm{tot}}} \omega_3 \sigma_{L_3}^{\mathrm{h}}, \tag{2}$$

$$\sigma_{L\alpha_{2,1}}^{\mathrm{x}} = \frac{\Gamma_{L_3 M_{4,5}}}{\Gamma_{3,\mathrm{tot}}} \omega_3 \sigma_{L_3}^{\mathrm{h}}, \tag{3}$$

$$\sigma_{L\eta}^{\mathrm{x}} = \frac{\Gamma_{L_2 M_1}}{\Gamma_{2,\mathrm{tot}}} \omega_2 \sigma_{L_2}^{\mathrm{h}}, \tag{4}$$

$$\sigma_{L\beta_6}^{\mathrm{x}} = \frac{\Gamma_{L_3 N_1}}{\Gamma_{3,\mathrm{tot}}} \omega_3 \sigma_{L_3}^{\mathrm{h}}, \tag{5}$$

$$\sigma_{L\beta_4}^{\mathrm{x}} = \frac{\Gamma_{L_1 M_2}}{\Gamma_{1,\mathrm{tot}}} \omega_1 \sigma_{L_1}^{\mathrm{h}}, \tag{6}$$

$$\sigma_{L\beta_{3,10,9,1,15,2}}^{\mathrm{x}} = \frac{\Gamma_{L_1 M_{3,4,5}}}{\Gamma_{1,\mathrm{tot}}} \omega_1 \sigma_{L_1}^{\mathrm{h}}$$
$$+ \frac{\Gamma_{L_2 M_4}}{\Gamma_{2,\mathrm{tot}}} \omega_2 \sigma_{L_2}^{\mathrm{h}} + \frac{\Gamma_{L_3 N_{4,5}}}{\Gamma_{3,\mathrm{tot}}} \omega_3 \sigma_{L_3}^{\mathrm{h}}, \tag{7}$$

$$\sigma_{L\beta_5}^{\mathrm{x}} = \frac{\Gamma_{L_3 O_{4,5}}}{\Gamma_{3,\mathrm{tot}}} \omega_3 \sigma_{L_3}^{\mathrm{h}}, \tag{8}$$

$$\sigma_{L\gamma_5}^{\mathrm{x}} = \frac{\Gamma_{L_2 N_1}}{\Gamma_{2,\mathrm{tot}}} \omega_2 \sigma_{L_2}^{\mathrm{h}}, \tag{9}$$

$$\sigma_{L\gamma_1}^{\mathrm{x}} = \frac{\Gamma_{L_2 N_4}}{\Gamma_{2,\mathrm{tot}}} \omega_2 \sigma_{L_2}^{\mathrm{h}}, \tag{10}$$

$$\sigma_{L\gamma_{2,3,6}}^{\mathrm{x}} = \frac{\Gamma_{L_1 N_{2,3}}}{\Gamma_{1,\mathrm{tot}}} \omega_1 \sigma_{L_1}^{\mathrm{h}} + \frac{\Gamma_{L_2 O_4}}{\Gamma_{2,\mathrm{tot}}} \omega_2 \sigma_{L_2}^{\mathrm{h}}, \tag{11}$$

$$\sigma_{L\gamma_{4,4'}}^{\mathrm{x}} = \frac{\Gamma_{L_1 O_{3,2}}}{\Gamma_{1,\mathrm{tot}}} \omega_1 \sigma_{L_1}^{\mathrm{h}}, \tag{12}$$

where ω_i is the fluorescence yield of subshell L_i, $\Gamma_{L_i(M,N,O)_j}$ is the emission rate for the radiative transition $L_i(M, N, O)_j$, and $\Gamma_{i,\mathrm{tot}}$ is the sum of the emission rates for all possible transitions to the L_i subshell.

In turn, the vacancy-production cross sections $\sigma_{L_i}^{\mathrm{h}}$ that appear in Eqs. (2) to (12) are related to the K, L_1, L_2, and L_3 ionization cross sections, namely, σ_K, σ_{L_1}, σ_{L_2}, and σ_{L_3}, respectively, by the system of linear equations

$$\sigma_{L_1}^{\mathrm{h}} = \sigma_{L_1} + \eta_{KL_1} \sigma_K, \tag{13}$$

$$\sigma_{L_2}^{\mathrm{h}} = \sigma_{L_2} + f_{12} \sigma_{L_1} + (\eta_{KL_2} + f_{12} \eta_{KL_1}) \sigma_K, \tag{14}$$

$$\sigma_{L_3}^{\mathrm{h}} = \sigma_{L_3} + f_{23} \sigma_{L_2} + (f_{13} + f'_{13} + f_{12} f_{23}) \sigma_{L_1}$$
$$+ (\eta_{KL_3} + f_{23} \eta_{KL_2}$$
$$+ (f_{13} + f'_{13} + f_{12} f_{23}) \eta_{KL_1}) \sigma_K, \tag{15}$$

where f_{ij} are the Coster-Kronig nonradiative transition probabilities, f'_{13} is the Coster-Kronig radiative transition probability, and η_{KL_i} are the vacancy-transfer probabilities from the K shell to the L_i subshells. The contribution of intrashell radiative transitions from L_1 to L_2 has not been included in Eqs. (14) and (15) because the corresponding yield f'_{12} is extremely small.

To determine σ_{L_1}, σ_{L_2}, and σ_{L_3} from the x-ray production cross sections of the aforementioned lines and multiplets we

have used the methodology presented in Ref. [29], which has already been applied in Ref. [12] to extract the Au L_i ionization cross sections. However, since the Bi L peaks are more resolved than those of Au L, and the peak fit procedure has been improved, we could select more individual lines to determine the Bi L_i ionization cross sections. In short, this procedure takes advantage of the fact that the x-ray production cross sections are linear in the ionization cross sections. Thus, the relationship between these two quantities can be written in the matrix form

$$\boldsymbol{\sigma}_0^{\mathrm{x}} = \mathbb{X} \boldsymbol{\sigma}_0, \tag{16}$$

with $\boldsymbol{\sigma}_0^{\mathrm{x}}$ a column vector with the true values of the x-ray production cross sections, $\boldsymbol{\sigma}_0$ a column vector with the true values of the L_1, L_2, and L_3 subshell ionization cross sections, and $\mathbb{X}$ a design matrix.

Taking the experimental values of the x-ray production cross sections $\boldsymbol{\sigma}_{\mathrm{expt}}^{\mathrm{x}}$ as an estimate for the true values that enter the vector $\boldsymbol{\sigma}_0^{\mathrm{x}}$ it is possible to estimate the values of the ionization cross sections in the vector $\boldsymbol{\sigma}_0$ with the least-squares method through the expression [29,46]

$$\hat{\boldsymbol{\sigma}} = \left(\mathbb{X}^{\mathrm{T}} \mathbb{V}_{\boldsymbol{\sigma}_{\mathrm{expt}}^{\mathrm{x}}}^{-1} \mathbb{X}\right)^{-1} \mathbb{X}^{\mathrm{T}} \mathbb{V}_{\boldsymbol{\sigma}_{\mathrm{expt}}^{\mathrm{x}}}^{-1} \boldsymbol{\sigma}_{\mathrm{expt}}^{\mathrm{x}}, \tag{17}$$

being $\hat{\boldsymbol{\sigma}}$ the column vector with the estimated values and $\mathbb{V}_{\boldsymbol{\sigma}_{\mathrm{expt}}^{\mathrm{x}}}$ the covariance matrix of the experimental values.

The design matrix $\mathbb{X}$ is constructed with the atomic relaxation parameters, which also have uncertainties that must be propagated to the variances of the fitted parameter vector. The total variance of $\hat{\boldsymbol{\sigma}}$ is given by [29]

$$\mathbb{V}_{\hat{\boldsymbol{\sigma}}} = \left(\mathbb{X}^{\mathrm{T}} \mathbb{V}_{\boldsymbol{\sigma}_{\mathrm{expt}}^{\mathrm{x}}}^{-1} \mathbb{X}\right)^{-1} + \mathbb{D} \, \mathbb{V}_{\mathrm{par}} \, \mathbb{D}^{\mathrm{T}}, \tag{18}$$

where the first term accounts for the uncertainties of the experimental x-ray production cross sections and the second one for the uncertainties of the atomic relaxation parameters. $\mathbb{V}_{\mathrm{par}}$ is the covariance matrix of the relaxation parameters and $\mathbb{D}$ is a rectangular matrix whose elements are the derivatives of the (sub)shell ionization cross sections with respect to each of these relaxation parameters. The covariances between the atomic relaxation parameters have been set to zero because, to the best of our knowledge, they have never been evaluated; hence, $\mathbb{V}_{\mathrm{par}}$ is a diagonal matrix.

If the energy of the electron beam is larger than the K-shell binding energy, $U_{\mathrm{Bi} K} = 90.5377(98)$ keV [33], migration of a K-shell vacancy to any L subshell must be contemplated. This condition was only met for the energy of 100.3(5) keV. In this single case the K-shell ionization cross section $\hat{\sigma}_K$ has been added to the vector $\hat{\boldsymbol{\sigma}}$ of parameters to be fitted, and the measured $K\alpha_{1,2}$ and $K\beta_{1,3}$ x-ray production cross sections have been included in the column vector $\boldsymbol{\sigma}_{\mathrm{expt}}^{\mathrm{x}}$. As the SDDs do not have enough efficiency above 50 keV, we have taken extrapolated values of the experimental data published in Ref. [13]. The values are 0.998(28) b and 0.216(18) b for $K\alpha_{1,2}$ and $K\beta_{1,3}$, respectively.

The average of the values of the x-ray production cross sections resulting from the measurements done with the two SDDs has been employed to determine the L_1, L_2, and L_3 ionization cross sections. These cross sections have been calculated using two data sets of atomic relaxation parameters, in order to evaluate the sensitivity of the ionization

TABLE I. Fluorescence yields and Coster-Kronig transition probabilities taken from Refs. [47] (set A) and [48] (set B). The standard deviation is given by the number in parentheses, in units of the least significant digit.

	ω_1	ω_2	ω_3	f_{12}	$f_{13} + f'_{13}$	f_{23}
Set A [47]	0.117(17)	0.387(19)	0.373(11)	0.110(11)	0.584(29)	0.113(17)
Set B [48]	0.11(3)	0.411(20)	0.353(18)	0.064(32)	0.62(9)	0.117(12)

cross sections to different parameter sets. These two sets have been named A and B. The fluorescence yields and Coster-Kronig coefficients, listed in Table I, have been taken from Refs. [47] (set A) and [48] (set B). The x-ray emission rates, collected in Table II, are from Refs. [42] (set A) and [43] (set B). In both sets the radiative and nonradiative vacancy-transfer probabilities from the K shell to the L_i subshells, needed just for 100.3(5) keV, have been taken from Refs. [42,49]; specifically, $\eta_{KL_1} = 0.00624(8)$, $\eta_{KL_2} = 0.296(21)$, and $\eta_{KL_3} = 0.497(34)$.

IV. THEORY

The SCADW formalism is based on first-order perturbation theory (Lorentz gauge) and it includes the full two-body retarded electromagnetic interaction. Relativistic (Dirac) distorted plane waves are adopted for all continuum electron states. This method was developed by Pindzola and his coworkers [17,18], and it has been used extensively to compute cross sections for electron-ion impact ionization in plasmas of interest to astrophysics and fusion research. More recently, the SCADW method has been applied successfully to the ionization of the inner (sub)shells of neutral atoms [20,21]. The mathematical expressions can be found in the original

publications [17,18] or in Ref. [13] and will not be repeated here.

Bote and Salvat [19] also employed the relativistic first Born approximation to perform systematic calculations of inner-shell ionization cross sections [6]. Their formalism starts from the Coulomb gauge wherein the electron-atom interaction is expressed as the sum of longitudinal and transverse contributions. The longitudinal term is evaluated using distorted plane waves for the initial and final wave functions of the projectile and target electrons. However, to simplify the expression of the transverse term, the projectile electron is described with plane waves. This calculation scheme is referred to as the DWBA. The transverse interaction is of the order of $(v/c)^2$; therefore, its effect is appreciable only for projectiles with relativistic velocities.

V. RESULTS

The experimental Bi $L\alpha$, $L\beta$, $L\gamma$, $L\ell$, and $L\eta$ x-ray production cross sections are exhibited in Fig. 8 together with the measurements of Refs. [23,24,28] and the theoretical values evaluated with the DWBA ionization cross sections [19,50] and the atomic relaxation parameters of sets A and B. The experimental x-ray production cross sections and their uncertainties are summarized in Table III; the tabulated values

TABLE II. *L*-subshell x-ray emission rates, in eV/$\hbar$ (1 eV/$\hbar$ = 1.519×10^{15} s^{-1}). The relative uncertainty (1 standard deviation) is estimated to be around 5% for set A [29], whereas it is less than 0.2% for set B [43].

		$\Gamma_{L_i(M,N,O)_j}$ (eV/$\hbar$)	
Line	Transition	Set A [42]	Set B [43]
$L\ell$	L_3M_1	0.0905	0.09113
$L\alpha_1$	L_3M_5	1.519	1.527
$L\alpha_2$	L_3M_4	0.1726	0.1740
$L\eta$	L_2M_1	0.0543	0.05549
$L\beta_6$	L_3N_1	0.02247	0.02292
$L\beta_4$	L_1M_2	0.486	0.4875
$L\beta_1$	L_2M_4	1.989	1.999
$L\beta_2$	L_3N_5	0.2951	0.3122
$L\beta_{15}$	L_3N_4	0.0326	0.03449
$L\beta_3$	L_1M_3	0.520	0.5242
$L\beta_9$	L_1M_5	0.02693	0.02693
$L\beta_{10}$	L_1M_4	0.01800	0.01800
$L\beta_5$	$L_3O_{4,5}$	0.0423	0.04856
$L\gamma_5$	L_2N_1	0.01408	0.01457
$L\gamma_1$	L_2N_4	0.411	0.4336
$L\gamma_2$	L_1N_2	0.1257	0.1290
$L\gamma_3$	L_1N_3	0.1474	0.1540
$L\gamma_6$	L_2O_4	0.0546	0.06257
$L\gamma_{4,4'}$	$L_1O_{3,2}$	0.0546	0.05722

TABLE III. Measured Bi $L\alpha$, $L\beta$, $L\gamma$, $L\ell$, and $L\eta$ x-ray production cross sections. The numbers between parentheses are the uncertainties (1 standard deviation) in units of the least significant digit.

| Energy (keV)	$\sigma^x_{L\alpha}$ (b)	$\sigma^x_{L\beta}$ (b)	$\sigma^x_{L\gamma}$ (b)	$\sigma^x_{L\ell}$ (b)	$\sigma^x_{L\eta}$ (b)
13.79(8)	10.6(6)	3.50(22)		0.46(5)	
14.45(7)	28.2(15)	7.2(4)		1.28(12)	
15.46(6)	48.7(26)	11.5(6)		2.44(16)	
16.07(7)	61(3)	18.1(9)	0.88(9)	3.17(19)	
17.74(5)	92(5)	44(2)	6.1(4)	4.72(27)	0.57(8)
18.46(6)	100(5)	52(3)	7.5(4)	5.25(28)	0.67(6)
20.76(6)	124(7)	75(4)	11.6(6)	6.7(4)	1.02(7)
22.19(8)	138(7)	84(4)	13.6(7)	7.3(4)	1.27(8)
26.01(4)	156(8)	101(5)	16.8(9)	8.4(5)	1.46(11)
27.92(5)	163(9)	106(6)	17.7(9)	8.6(5)	1.61(11)
30.89(4)	170(9)	113(6)	19.1(10)	8.9(5)	1.66(11)
40.61(8)	174(9)	120(6)	20.8(11)	9.0(5)	1.83(15)
50.3(5)	166(9)	116(6)	19.9(11)	8.9(5)	1.80(13)
61.0(5)	164(9)	115(6)	19.8(11)	8.6(5)	1.65(11)
70.7(5)	153(8)	109(6)	18.9(10)	8.1(4)	1.62(10)
80.7(5)	154(8)	110(6)	19.0(10)	8.1(4)	1.62(10)
90.4(5)	148(8)	106(6)	18.4(10)	7.9(4)	1.63(10)
100.3(5)	139(8)	101(5)	17.6(9)	7.4(4)	1.48(9)
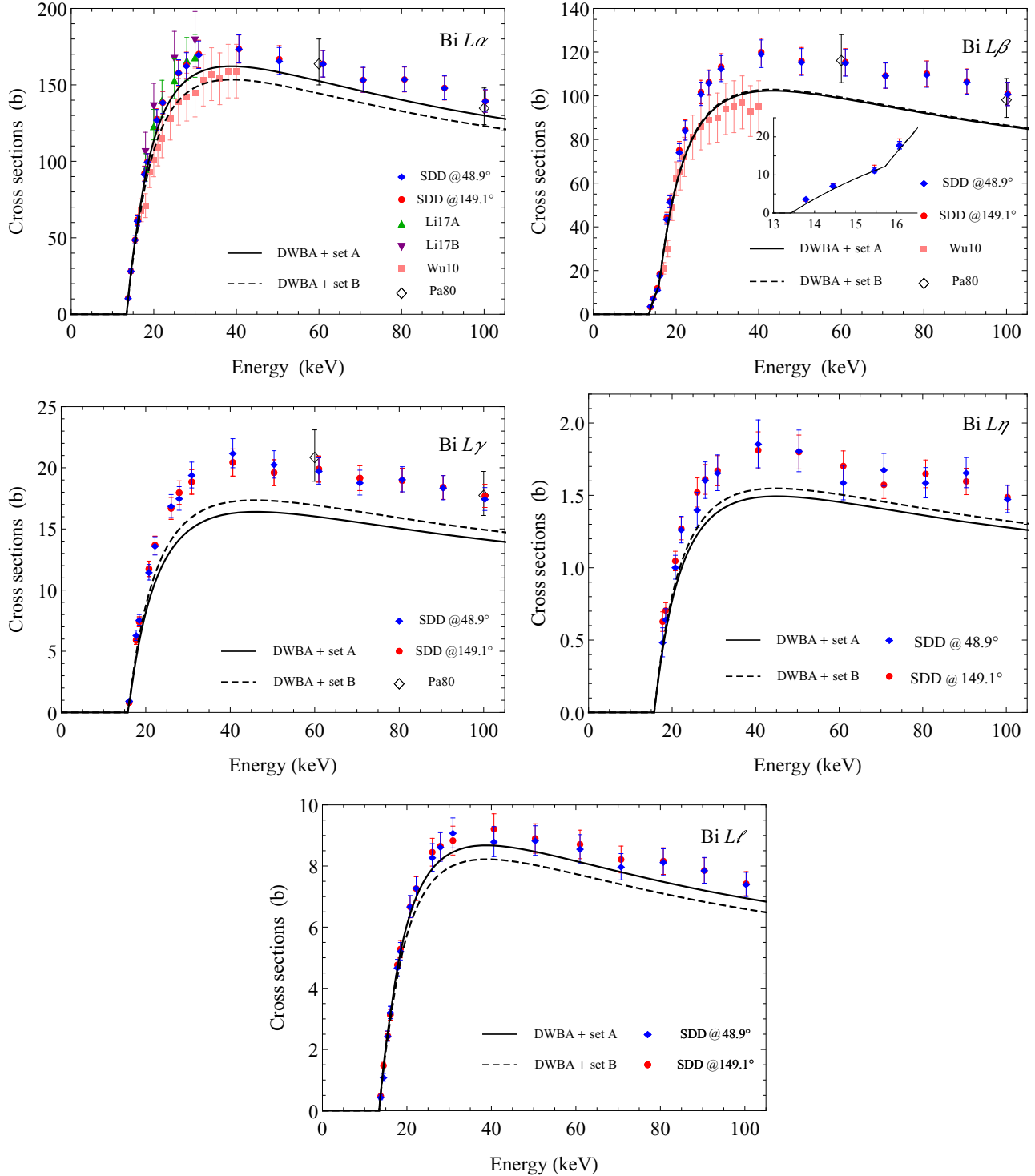
FIG. 8. Bi $L\alpha$, $L\beta$, $L\gamma$, $L\ell$, and $L\eta$ x-ray production cross sections. The (blue) diamonds and (red) circles are our experimental values for the detectors placed at $48.9(5)°$ and $149.1(5)°$ relative to the incident beam direction, respectively. The uncertainty bars correspond to 1 standard deviation. The (black) empty diamonds, (pink) squares, (green) up triangles, and (purple) down triangles represent the data from Refs. Pa80 [28], Wu10 [23], Li17A [24] (thin substrate), and Li17B [24] (thick substrate), respectively. The continuous and dashed curves indicate the theoretical DWBA results combined with atomic relaxation parameters from sets A and B, respectively.

correspond to the average of the measurements done at the two angles.

Figure 9 compares the present Bi L_1, L_2, and L_3 subshell ionization cross sections with the experimental values from Ref. [28] and the predictions of the DWBA [19,50] and SCADW formalisms [17,18,20]. Our measured cross sections are also listed in Table IV. The *relative* Bi L_3 ionization cross section is shown in Fig. 10 and compared to the data reported in Ref. [22] and to the theoretical curves.
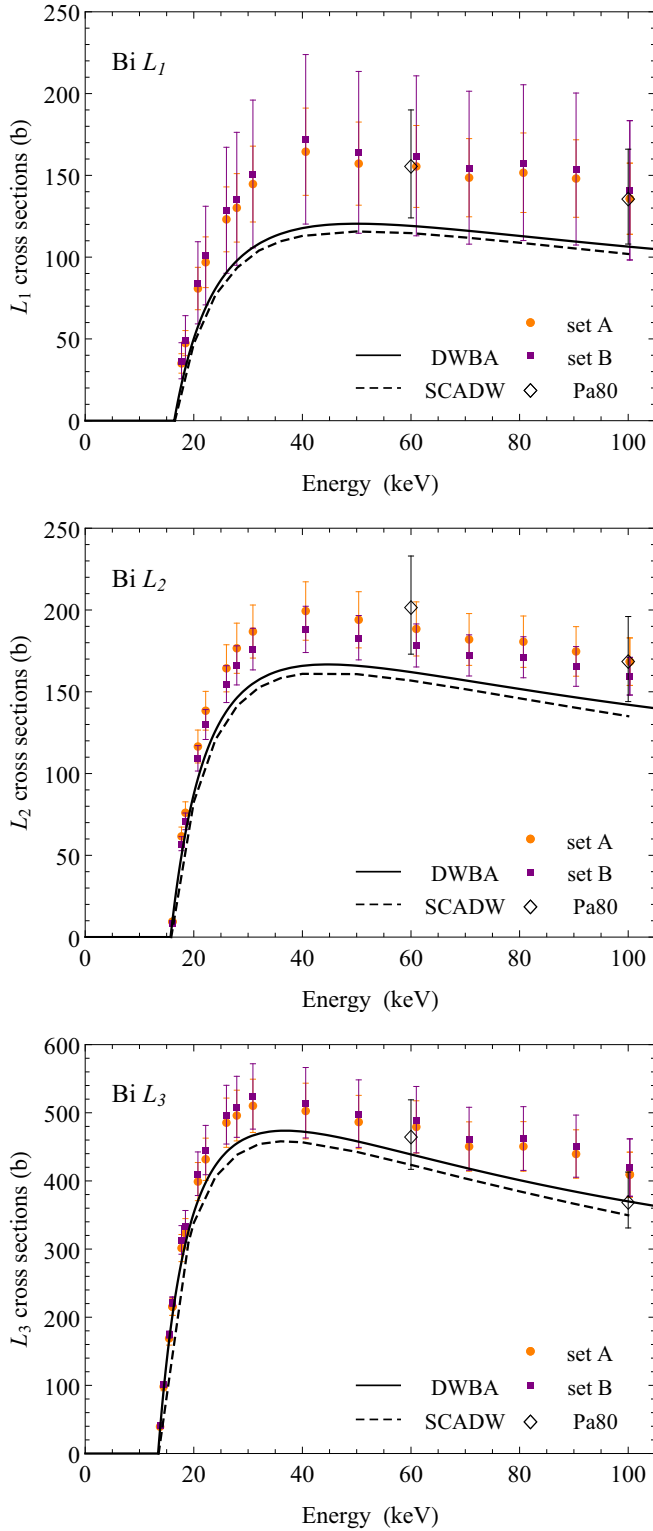
FIG. 9. Experimental Bi L_1, L_2, and L_3 subshell ionization cross sections. The full symbols are the present values, determined with atomic relaxation parameters from set A (orange circles) and set B (purple squares). The uncertainty bars correspond to 1 standard deviation. The (black) empty diamonds represent the data from Ref. Pa80 [28]. The continuous and dashed curves are theoretical cross sections calculated with the DWBA [19,50] and SCADW [17,18,20] formalisms, respectively.

TABLE IV. Experimental Bi L_1, L_2, and L_3 subshell ionization cross sections. The numbers between parentheses are the uncertainties (1 standard deviation) in units of the least significant digit.

Energy (keV)	σ_{L_1} (b)	σ_{L_2} (b)	σ_{L_3} (b)
13.79(8)			39.3(25)
14.45(7)			98(6)
15.46(6)			169(10)
16.07(7)		9.4(11)	215(13)
17.74(5)	35(6)	62(6)	301(20)
18.46(6)	47(8)	76(7)	323(21)
20.76(6)	81(13)	117(10)	399(28)
22.19(8)	97(16)	138(12)	432(31)
26.01(4)	123(20)	164(14)	485(36)
27.92(5)	130(21)	177(15)	496(37)
30.89(4)	145(23)	187(16)	510(39)
40.61(8)	164(27)	199(18)	503(41)
50.3(5)	157(25)	194(17)	486(39)
61.0(5)	155(25)	188(17)	479(38)
70.7(5)	149(24)	182(16)	450(36)
80.7(5)	151(24)	181(16)	451(36)
90.4(5)	148(24)	175(15)	439(35)
100.3(5)	136(22)	168(15)	409(33)

VI. DISCUSSION

A. L x-ray production cross sections

We have refined the procedure developed in Refs. [12,29] to fit the parameters of the L multiplet, fitting in a single step the parameters of the $L\ell$ and $L\eta$ lines and those of the $L\alpha$, $L\beta$, and $L\gamma$ multiplets. The comparison of the measurements taken simultaneously with detectors at two angles enables a better evaluation of the estimated peak areas because the
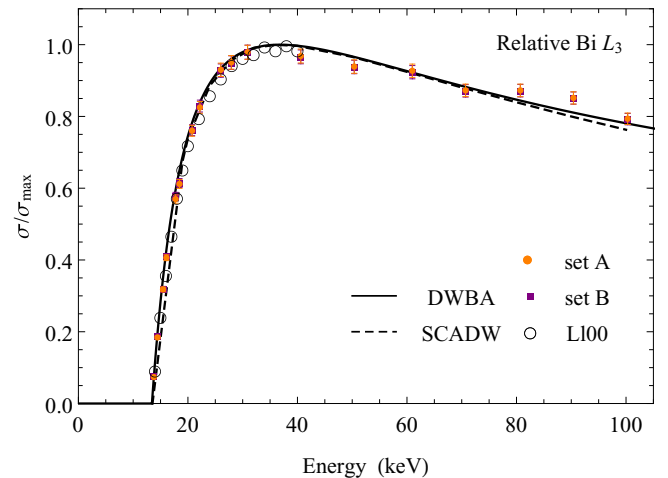

FIG. 10. Energy dependence of the measured and calculated Bi L_3 ionization cross sections, normalized to the maximum height. The full symbols are the present values, determined with atomic relaxation parameters from set A (orange circles) and set B (purple squares). The (black) empty circles denote the data from Ref. Ll00 [22]. The continuous and dashed curves are, respectively, the normalized DWBA [19,50] and SCADW [17,18,20] L_3 ionization cross sections.

intensities of the continuous components in the respective spectra are quite different due to the strong angular dependence of bremsstrahlung emission (see Fig. 4), while the intensities of the characteristic x-ray peaks are expected to be similar within the uncertainty bars.

Our Bi $L\alpha$, $L\beta$, $L\gamma$, $L\ell$, and $L\eta$ x-ray production cross sections, plotted in Fig. 8, agree with the existing experimental data of Refs. [23,24] ($\sigma_{L\alpha}^x$ and $\sigma_{L\beta}^x$ between 17 and 40 keV) and [28] ($\sigma_{L\alpha}^x$, $\sigma_{L\beta}^x$, and $\sigma_{L\gamma}^x$ at 60 and 100 keV). Nevertheless, our overall uncertainties are around 5%, 5%, 6%, 7%, and 9%, respectively, which constitutes a substantial improvement in the accuracy compared to the data available for Bi, and even better than other recent measurements of x-ray production cross sections of high-Z elements [10,51].

Pálinkás and Schlenk [28] employed a Si(Li) spectrometer with FWHM equal to 194 eV at 6.4 keV to detect the $L\alpha$, $L\beta$, and $L\gamma$ x rays emitted by thin Bi films whose mass thicknesses were between 20 and 200 μg/cm^2 irradiated with 60 to 600 keV electrons. In the measurements by Wu *et al.* [23] the x rays emitted from a thin Bi film (mass thickness 10.7 μg/cm^2) deposited on a thick C substrate were recorded by a Si(Li) detector with energy resolution of 170 eV at 5.9 keV. These authors reported $L\alpha$ and $L\beta$ x-ray production cross sections between 17 and 40 keV. More recently, Liang *et al.* [24] conducted an experiment using two targets: an ultrathin Bi film deposited on a self-supporting C film ($\approx$60 nm), and an ultrathin Bi film deposited onto a highly pure, thick C substrate. The mass thickness of the Bi films was around 7.5 μg/cm^2, and the x rays were detected with an SDD whose resolution was not quoted. The $L\alpha$ x-ray production cross sections were measured between 15 and 30 keV. Our measurements have, therefore, the smallest corrections for the finite thickness of the target and of the backing because here the thicknesses of these are smaller than those used in the earlier experiments.

The lines in the $L\beta$ multiplet originate from vacancies created in the three L subshells. The good precision of our results in conjunction with the choice of a few electron beam energies near the L_1, L_2, and L_3 ionization thresholds allowed us to visualize the change in the slope of the experimental $\sigma_{L\beta}^x$ curve when only L_3 is ionized, and then when the energy of the beam is sufficient to ionize the three L subshells. This behavior is well reproduced by the theoretical curves calculated from the DWBA using sets A and B [inset of Fig. 8(b)].

Comparing the curves calculated with the DWBA and the two sets of atomic relaxation parameters it is concluded that the theoretical x-ray production cross sections are sensitive to the choice of these parameters. The measured values of $\sigma_{L\ell}^x$ and $\sigma_{L\alpha}^x$ lie around 5% and 10% above the DWBA curves calculated with sets A and B, respectively. For $L\beta$, the curves calculated with both sets almost coincide, and they underestimate our cross sections by approximately 13%. The experimental $L\gamma$ and $L\eta$ x-ray production cross sections are about 14% above the curve calculated with set B and 23% above that calculated with set A. Hence, the concordance between experiment and theory for $L\ell$ and $L\alpha$ does not happen for $L\beta$, $L\gamma$, and $L\eta$, and for these latter the theoretical predictions determined with the two sets of atomic relaxation parameters underestimate the experimental data, with the greatest departure for $L\gamma$ and $L\eta$.

As already mentioned, the measured ratios of peak areas corrected for the FE peak efficiency are consistent with the theoretical ratios, Fig. 6. Consequently, the discrepancies between the experimental and theoretical x-ray production cross sections should come either from the formalism used to calculate the ionization cross sections, or from the fluorescence yields and Coster-Kronig coefficients. Our results for $L\ell$ and $L\alpha$, and the smallest disagreement between theory and experiment for $L\beta$ as compared to $L\gamma$ and $L\eta$ suggest that the reason for the mismatch could be either in the theoretical L_1 or L_2 ionization cross sections, or in the relaxation parameters of these subshells.

B. *L*-subshell ionization cross sections

The Bi L_1, L_2, and L_3 subshell ionization cross sections have been estimated with global uncertainties [Eq. (18)], equal to 17%, 9%, and 8%, respectively, when the atomic relaxation parameters from set A were used, and equal to 31%, 7%, and 9% when the parameters from set B were adopted (1 standard deviation). However, the experimental uncertainties, which exclude the uncertainties of the relaxation parameters [second term in the right-hand side of Eq. (18)], are 5%, 4%, and 4% for σ_{L_1}, σ_{L_2}, and σ_{L_3}, respectively.

Despite having reduced the uncertainties of our x-ray production cross sections by almost a factor of 2 with respect to the data from Ref. [28], the improvement in the accuracy of the ionization cross sections has been modest. This is due to the uncertainties of the atomic relaxation parameters. For the cross sections determined with the parameters of set A, a slightly better precision has been achieved with respect to the measurements of Ref. [28] owing to the improvements in the experimental arrangement and data analysis methodology. In the case of the measurements with set B, the precision of the experimental results is better only for the L_2 ionization cross sections. Even though the transition rates of set B are more accurate than those of set A, the uncertainties of the parameters recommended for Bi in Ref. [48] are high, reaching 50% for f_{12} and 30% for ω_1, thus worsening the accuracy of σ_{L_1}.

Recently, we have measured Au L_1, L_2, and L_3 ionization cross sections [12]. The experimental uncertainties were larger than those reported here, but the final uncertainties, including the contribution from the atomic relaxation parameters, were better than those in this paper. This is because for Au there are measurements of fluorescence yields and Coster-Kronig coefficients [52], with higher precision than those of Refs. [42,48]. The uncertainty of ω_1, for example, is 3.5%, which allowed obtaining the Au L_1 ionization cross section with a relative uncertainty of 8%.

As seen in Fig. 9, the present L_1, L_2, and L_3 subshell ionization cross sections are consistent with those measured at 60 and 100 keV by Pálinkás and Schlenk [28]. These authors employed the method denoted as TRY3 in Cohen's review [53], which uses the $L\alpha_{1,2}$, $L\gamma_1$, and $L\gamma_{2,3,6}$ x-ray production cross sections to deduce σ_{L_1}, σ_{L_2}, and σ_{L_3}. The relaxation data were taken from set A. A comparison of the ionization cross sections obtained with the methods analyzed by Cohen, including TRY3, with those ensuing from the procedure proposed here can be found in Ref. [29].

The experimental and theoretical subshell ionization cross sections are in satisfactory agreement, but for the L_1 subshell this is so because the uncertainties are large. The data for σ_{L_1} are approximately 33% above the theoretical curve. However, the experimental uncertainties for these measurements reach 31% in the case of set B since the uncertainty in ω_1 is 30%. Furthermore, our relative L_3 ionization cross sections are in excellent accord with those of Ref. [22], and also with the calculations performed with the two theoretical formalisms studied here.

From the experimental point of view, if the target thickness were evaluated incorrectly, the absolute cross sections would be underestimated or overestimated. In this kind of situation the L_1, L_2, and L_3 ionization cross sections would be rescaled by the same multiplicative factor, which is not observed in the present data, where the theoretical values underestimate σ_{L_1} by 35% and σ_{L_3} by a mere 6%.

VII. CONCLUSIONS

We have measured and calculated Bi L_1, L_2, and L_3 ionization cross sections from the L_3 ionization threshold up to 100 keV. The experimental values have been deduced from the measured Bi *L* x-ray production cross sections, whose relative standard deviations are in the range $5\% - 9\%$. The total uncertainty of the experimental σ_{L_2} and σ_{L_3} values is less than 10%, but in the case of σ_{L_1} the total uncertainty reaches 17% and 31% depending on whether the atomic relaxation parameters are taken from set A or set B, respectively. The large uncertainty of the fluorescence yield ω_1 of Bi, especially in set B, is responsible for this loss of accuracy. Although the agreement between theory and experiment is reasonable for the three *L* subshells, the ionization cross sections presently computed with the SCADW formalism underestimate the data, and the same trend is followed by the simpler DWBA.

[1] C. J. Powell, Rev. Mod. Phys. **48**, 33 (1976).

[2] C. J. Powell, *Electron Impact Ionization*, edited by T. D. Märk and G. H. Dunn (Springer, Wien, 1985), pp. 198–231.

[3] F. Salvat, PENELOPE-2018: A Code System for Monte Carlo Simulation of Electron and Photon Transport (Issy-les-Moulineaux, OECD/NEA, 2019).

[4] J. R. Davies, R. Betti, P. M. Nilson, and A. A. Solodov, Phys. Plasmas **20**, 083118 (2013).

[5] P. Palmeri, P. Quinet, and D. Batani, At. Data Nucl. Data Tables **102**, 1 (2015).

[6] X. Llovet, C. J. Powell, F. Salvat, and A. Jablonski, J. Phys. Chem. Ref. Data **43**, 013102 (2014).

[7] J. C. Clark, Phys. Rev. **48**, 30 (1935).

[8] S. L. Salem and L. D. Moreland, Phys. Lett. A **37**, 161 (1971).

[9] C. S. Campos, M. A. Z. Vasconcellos, X. Llovet, and F. Salvat, Phys. Rev. A **66**, 012719 (2002).

[10] H. V. Rahangdale, M. Guerra, P. K. Das, S. De, J. P. Santos, D. Mitra, and S. Saha, Phys. Rev. A **89**, 052708 (2014).

[11] J. L. Zhao, Z. An, J. J. Zhu, W. J. Tan, and M. T. Liu, J. Phys. B: At., Mol. Opt. Phys. **49**, 065205 (2016).

[12] S. F. Barros, V. R. Vanin, N. L. Maidana, M. N. Martins, J. A. García-Alvarez, O. C. B. Santos, C. L. Rodrigues, M. F. Koskinas, and J. M. Fernández-Varea, J. Phys. B: At., Mol. Opt. Phys. **51**, 025201 (2018).

[13] O. C. B. Santos, V. R. Vanin, N. L. Maidana, M. N. Martins, M. H. Tabacniks, C. L. Rodrigues, T. F. Silva, A. D. Santos, S. F. Barros, J. A. García-Alvarez, M. F. Koskinas, J. M. Fernández-Varea, and M. S. Pindzola, Phys. Rev. A **100**, 022703 (2019).

[14] J. L. Zhao, S. Bai, Z. An, J. J. Zhu, W. J. Tan, and M. L. Liu, Radiat. Phys. Chem. **171**, 108722 (2020).

[15] A. Carreras, G. Castellano, S. Segui, and J. Trincavelli, Phys. Rev. A **102**, 012817 (2020).

[16] V. R. Vanin, N. L. Maidana, A. Mangiarotti, R. R. Lima, A. A. Malafronte, S. F. Barros, and M. N. Martins, Radiat. Phys. Chem. **154**, 26 (2019).

[17] M. S. Pindzola and M. J. Buie, Phys. Rev. A **37**, 3232 (1988).

[18] M. S. Pindzola, D. L. Moores, and D. C. Griffin, Phys. Rev. A **40**, 4941 (1989).

[19] D. Bote and F. Salvat, Phys. Rev. A **77**, 042701 (2008).

[20] M. S. Pindzola, J. Phys. B: At., Mol. Opt. Phys. **48**, 015201 (2015).

[21] M. S. Pindzola, Phys. Rev. A **90**, 022708 (2014).

[22] X. Llovet, C. Merlet, J. M. Fernández-Varea, and F. Salvat, Mikrochim Acta **132**, 163 (2000).

[23] Y. Wu, Z. An, Y. M. Duan, and M. T. Liu, Nucl. Instrum. Methods Phys. Res., Sect. B **268**, 2473 (2010).

[24] Y. Liang, M. X. Xu, Y. Yuan, Y. Wu, Z. C. Qian, C. H. Chang, C. S. Mei, J. J. Zhu, and K. Moharram, Radiat. Phys. Chem. **141**, 17 (2017).

[25] L. M. Middleman, R. L. Ford, and R. Hofstadter, Phys. Rev. A **2**, 1429 (1970).

[26] Y. K. Park, M. T. Smith, and W. Scholz, Phys. Rev. A **12**, 1358 (1975).

[27] S. Ricz, B. Schlenk, D. Benényi, A. Valek, G. Hock, and S. A. H. Seif el Nasr, J. Phys. B: At. Mol. Phys. **11**, 4283 (1978).

[28] J. Pálinkás and B. Schlenk, Z. Phys. A **297**, 29 (1980).

[29] S. F. Barros, V. R. Vanin, N. L. Maidana, and J. M. Fernández-Varea, J. Phys. B: At., Mol. Opt. Phys. **48**, 175201 (2015).

[30] S. F. Barros, V. R. Vanin, A. Mangiarotti, N. L. Maidana, and J. M. Fernández-Varea, Phys. Rev. A **100**, 062705 (2019).

[31] T. F. Silva, C. L. Rodrigues, M. Mayer, M. V. Moro, G. F. Trindade, F. R. Aguirre, N. Added, M. A. Rizzutto, and M. H. Tabacniks, Nucl. Instrum. Methods Phys. Res., Sect. B **371**, 86 (2016).

[32] M. Mayer, in *The Fifteenth International Conference on the Application of Accelerators in Research and Industry*, AIP Conference Proceedings, Volume 475 (AIP, Melville, NY, 1999), p. 541.

[33] R. D. Deslattes, E. G. Kessler Jr, P. Indelicato, L. de Billy, E. Lindroth, and J. Anton, Rev. Mod. Phys. **75**, 35 (2003).

[34] S. F. Barros, N. L. Maidana, J. M. Fernández-Varea, and V. R. Vanin, X-Ray Spectrom. **46**, 34 (2017).

[35] S. M. Seltzer, Nucl. Instrum. Methods **188**, 133 (1981).

[36] S. F. Barros, V. R. Vanin, A. A. Malafronte, N. L. Maidana, and M. N. Martins, J. Synchrotron Radiat. **25**, 484 (2018).

[37] J. M. Fernández-Varea, V. Jahnke, N. L. Maidana, A. A. Malafronte, and V. R. Vanin, J. Phys. B: At., Mol. Opt. Phys. **47**, 155201 (2014).

[38] S. M. Seltzer and M. J. Berger, At. Data Nucl. Data Tables **35**, 345 (1986).

[39] L. Kissel, C. A. Quarles, and R. H. Pratt, At. Data Nucl. Data Tables **28**, 381 (1983).

[40] F. Gao, L. W. Campbell, R. Devanathan, Y. L. Xie, Y. Zhang, A. J. Peurrung, and W. J. Weber, Nucl. Instrum. Methods Phys. Res., Sect. A **579**, 292 (2007).

[41] M. O. Krause and J. H. Oliver, J. Phys. Chem. Ref. Data **8**, 329 (1979).

[42] J. H. Scofield, At. Data Nucl. Data Tables **14**, 121 (1974).

[43] J. L. Campbell and J. X. Wang, At. Data Nucl. Data Tables **43**, 281 (1989).

[44] M. J. Berger, A. Jablonski, I. K. Bronić, J. Mitroy, C. J. Powell, F. Salvat, and L. Sanche, Journal of the International Commission on Radiation Units and Measurements, 7 (2007).

[45] E. G. Berezhko and N. M. Kabachnik, J. Phys. B: At. Mol. Phys. **10**, 2467 (1977).

[46] W. T. Eadie, D. Drijard, E. F. James, M. Roos, and B. Sadoulet, *Statistical Methods in Experimental Physics* (North Holland, Amsterdam, 1971).

[47] M. O. Krause, J. Phys. Chem. Ref. Data **8**, 307 (1979).

[48] J. L. Campbell, At. Data Nucl. Data Tables **85**, 291 (2003).

[49] P. V. Rao, Phys. Rev. A **5**, 997 (1972).

[50] X. Llovet, F. Salvat, D. Bote, F. Salvat-Pujol, A. Jablonski, and C. J. Powell, NIST Database of Cross Sections for Inner-Shell Ionization by Electron or Positron Impact, Version 1.0 NIST Standard Reference Database 164, 2014, http://dx.doi.org/10.6028/NIST.NSRDS.164

[51] A. Moy, C. Merlet, X. Llovet, and O. Dugne, J. Phys. B: At., Mol. Opt. Phys. **46**, 115202 (2013).

[52] M. Kolbe, P. Hönicke, M. Müller, and B. Beckhoff, Phys. Rev. A **86**, 042512 (2012).

[53] D. D. Cohen, J. Phys. B: At. Mol. Phys. **17**, 3913 (1984).